Konrad-Zuse-Zentrum
für Informationstechnik Berlin

Takustraße 7
D-14195 Berlin-Dahlem
Germany

C. KOBER [1] B. ERDMANN
R. SADER H.–F. ZEILHOFER

Simulation of the Human Mandible: Comparison of Bone Mineral Density and Stress/Strain Profiles due to Masticatory Muscles' Traction

[1]submitted to Proceedings of the 10th workshop "The Finite Element Method in Biomedical Engineering, Biomechanics and Related Fields", Ulm, July 17 – 18, 2003

Simulation of the Human Mandible: Comparison of Bone Mineral Density and Stress/Strain Profiles due to Masticatory Muscles' Traction

Cornelia Kober[1] Bodo Erdmann[2]
Robert Sader[3] Hans–Florian Zeilhofer[3]

Abstract

The correlation of the inner architecture of bone and its functional loading was already stated by Wolff in 1892. Our objective is to demonstrate this interdependence in the case of the human mandible. For this purpose, stress/strain profiles occurring at a human lateral bite are simulated. Additionally, by a combination of computer graphics modules, a three–dimensional volumetric visualization of bone mineral density can be given.
Qualitative correspondences of the density profile of the jaw to the simulated stress/strain profiles are pointed out. In the long run, this might enable the use of the simulation for diagnosis and prognosis.
The solution of the underlying partial differential equations describing linear elastic material behaviour is provided by an adaptive finite element method. Estimates of the discretization errors, local grid refinement, and multilevel techniques guarantee the reliability and efficiency of the method.

1 Introduction

"Every change in the form and function of bones, or of their function alone, is followed by certain definite changes in their internal architecture and equally

[1]FH Osnabrück, TU München (HFZ)
[2]Konrad-Zuse-Zentrum für Informationstechnik Berlin
[3]University Hospital Basel, TU München (HFZ)

definite secondary alteration in their external conformation, in accordance with mathematical laws."

These are the original terms of the famous Wolff's law about the interdependence between the inner architecture of bone and its functional loading which was already stated in 1892 [22].

On the one hand, modern simulation techniques, mostly using finite element methods, enable reliable and efficient computation of stress and strain profiles and thus a detailed analysis of the loading situation [7].

On the other hand, recent visualization approaches of the authors deliver a macroscopic volumetric profile of the inner structure due to the optical density accessible via the Hounsfield values coming from ct–data [12].

In this article, we combine these two approaches in a pilot study concerning the human mandible. Muscular activity is one of the most important physiological loads bone is exposed to. The masticatory muscles are one of the strongest in the human body. We want to study whether we can point out a correlation of stress/strain profile due to these muscles and the inner structure of the mandible.

In a sense, this study contributes also to a vice versa validation of both, the simulation model and the density visualization techniques presented in [12].

2 Materials and Methods

2.1 Segmentation and surface reconstruction

We choose the partially edentulous mandible of the female visible human [2] as first test example, because of the extensive information on soft tissue by the anatomical images additional to ct– and mri–data and its very elaborate documentation in the literature.

A segmentation of the concerned tissues is a prerequisite for the simulation and for the visualization of the inner structure. This includes the mandible with cortical shell and cancellous core separated, the teeth, the eight masticatory muscles (four on each side), and two simplified temporo mandibular joint capsules. For description of the anatomical details, see Figure 1.

The segmentation of muscular tissue only on behalf of ct–data is quite tedious and thus less reliable. Therefore, the first step is a superposition of the ct–data and the anatomical images [11]. Using the semiautomatic tools

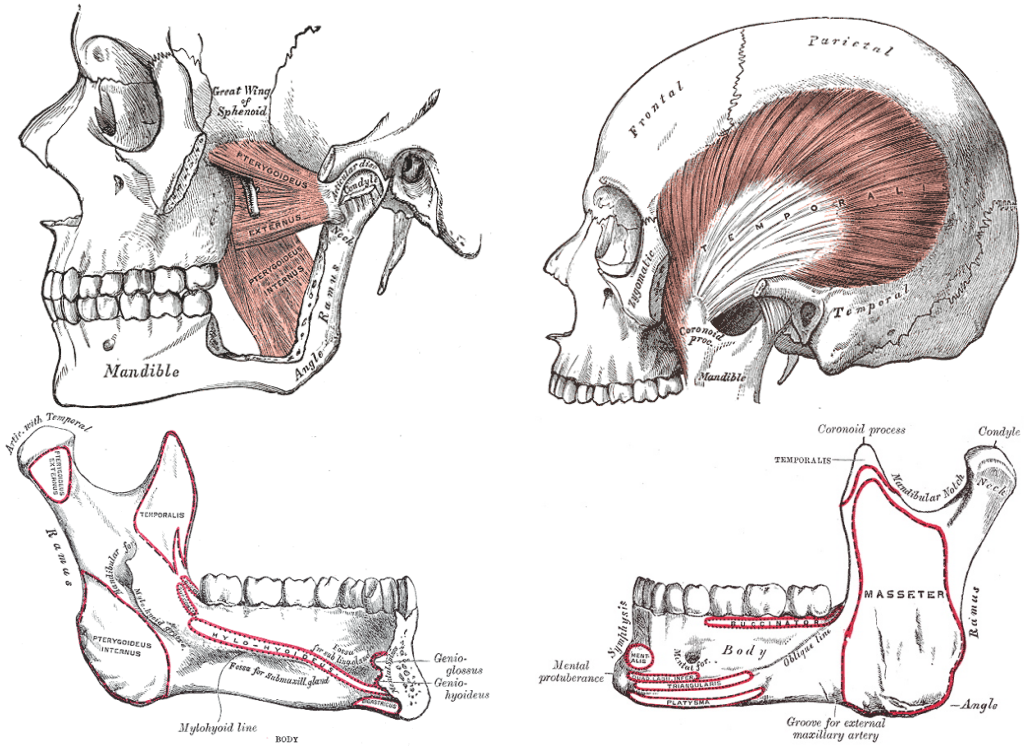

Figure 1: The anatomy of the mandible and the masticatory system [8].

provided by the visualization toolbox AMIRA 3.0 [20], it is possible to perform the necessary hard and soft tissue segmentation. Based on this input, the AMIRA built–in algorithm for generation of non–manifold surfaces gives a quite satisfactory reconstruction of the individual geometry. For the theoretical background, we refer to [16, 18, 19].

The complete model is shown in Figure 2. The cortical shell of the mandible, its inside spongy bone, the teeth, the masticatory system (musculi masseter, temporalis, pterygoidei mediales, pterygoidei laterales), and the two simplified temporo mandibular joint (tmj) capsules are separate geometric entities. For a detailed view of the muscles and the capsules, see Figure 4.

The jaw bone, the teeth, and the temporo mandibular joint capsules are modeled in our finite element simulation by a tetrahedral grid whereas the muscle forces are considered as boundary conditions. The grid generated for the mandibular surface (Figure 2) contains about 300,000 points which is too much for an efficient numerical treatment as described in the next section. Therefore, further preprocessing has to be performed. By successive grid coarsening, smoothing, and interactive improvement a surface mesh of

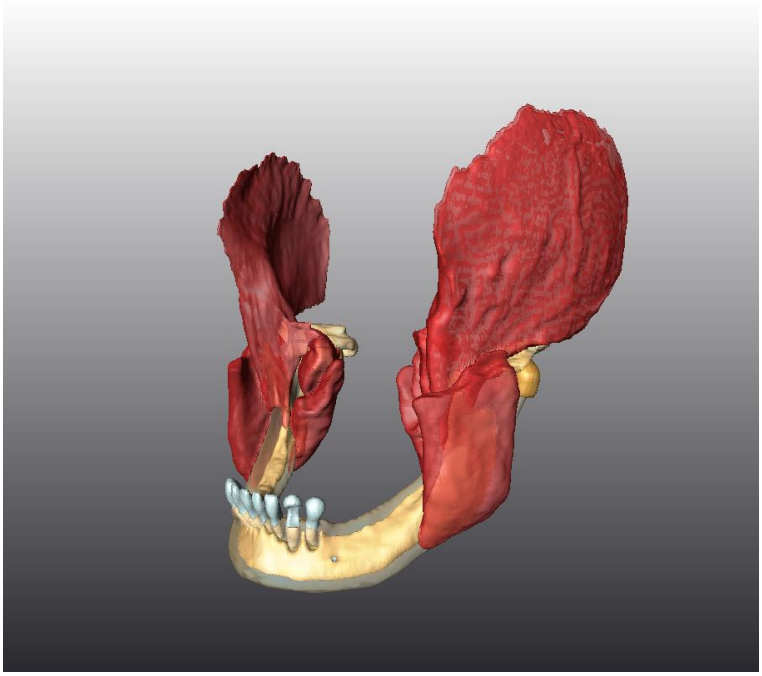

Figure 2: Surface reconstruction.

sufficient quality for volumetric mesh generation can be achieved. See [7, 18, 19] for details.

2.2 Numerical background: adaptive finite elements

In our study of the human mandible, the governing physical laws are the three–dimensional equations of linear elasticity:

$$-\mu\nabla\cdot(\nabla u+(\nabla u)^T)-\lambda\nabla(\nabla\cdot u) \;=\; 0 \qquad (1)$$

completed by boundary values. u denotes the displacement vector. λ and μ are the Lamé constants which fulfill the relations

$$\mu=\tfrac{E}{2(1+\nu)},\ \lambda=\tfrac{E\nu}{(1+\nu)(1-2\nu)}$$

with Young modulus E and Poisson number ν.

If we introduce the stress tensor $\sigma:=(\sigma_{ij})$ and the strain tensor $\epsilon:=(\epsilon_{ij})=(\nabla u+(\nabla u)^T)/2$, $1\leqslant i,j\leqslant 3$, we get for isotropic materials

$$\begin{pmatrix} \sigma_{11} \\ \sigma_{22} \\ \sigma_{33} \\ \sigma_{12} \\ \sigma_{13} \\ \sigma_{23} \end{pmatrix} = \mathcal{C} \begin{pmatrix} \varepsilon_{11} \\ \varepsilon_{22} \\ \varepsilon_{33} \\ 2\varepsilon_{12} \\ 2\varepsilon_{13} \\ 2\varepsilon_{23} \end{pmatrix} \tag{2}$$

with the matrix of elastic coefficients

$$\mathcal{C} = \frac{E}{(1+\nu)(1-2\nu)} \begin{pmatrix} 1-\nu & \nu & \nu & 0 & 0 & 0 \\ \nu & 1-\nu & \nu & 0 & 0 & 0 \\ \nu & \nu & 1-\nu & 0 & 0 & 0 \\ 0 & 0 & 0 & \frac{(1-2\nu)}{2} & 0 & 0 \\ 0 & 0 & 0 & 0 & \frac{(1-2\nu)}{2} & 0 \\ 0 & 0 & 0 & 0 & 0 & \frac{(1-2\nu)}{2} \end{pmatrix}$$

Equation 1 is equivalent to

$$div\ \sigma = 0 \tag{3}$$

We are using linear finite element methods with tetrahedral meshes for the numerical solution of these stationary partial differential equations. Tetrahedral meshes allow us to get a faithful representation of the complicated tissue boundaries. The generation of such grids is a difficult task, often a lot of manual support is necessary. Our mandible grids are provided by the visualization software AMIRA, see [20] and for the theoretical background [16, 18, 19, 17].

Typically, for a given application, we try to obtain a result via an efficient reliable simulation. Therefore, our finite element algorithms are based on adaptive mesh refinement [5, 4, 13], i.e., the finite element grid is automatically improved in regions where the numerical solution does not have the required accuracy. Adaptive techniques are driven by error estimators, which yield an estimate of the local discretization error in the calculated variables (here the displacement vector). This kind of a posteriori error estimation is based on hierarchical space extensions, i.e., by local comparison of the linear

finite element solution with local quantities computed as approximate residuals on small subdomains employing quadratic finite elements. Thus the user is released from constructing problem–specific discretizations.

Adaptive techniques are playing an increasingly important role in the area of computational science. Numerical and modelling errors can be clearly distinguished with the effect that reliability of the modelling process can be assessed. Compared to methods using only uniform refinement, successful adaptive methods lead to substantial savings in computational work for a given error tolerance.

Efficient implementation of adaptive mesh refinement requires particular attention to the supporting data structures and algorithm complexity [6]. The described algorithms are implemented in the FEM–code KASKADE ([5], [4], [1]).

Using KASKADE the equations 1 or 3 have to be transformed into the shape

$$-\nabla \cdot (\mathbf{D}\nabla u) = 0 \tag{4}$$

with

$$\mathbf{D} = \begin{pmatrix} \begin{pmatrix} \lambda+2\mu & 0 & 0 \\ 0 & \mu & 0 \\ 0 & 0 & \mu \end{pmatrix} & \begin{pmatrix} 0 & \lambda & 0 \\ \mu & 0 & 0 \\ 0 & 0 & 0 \end{pmatrix} & \begin{pmatrix} 0 & 0 & \lambda \\ 0 & 0 & 0 \\ \mu & 0 & 0 \end{pmatrix} \\ \begin{pmatrix} 0 & \mu & 0 \\ \lambda & 0 & 0 \\ 0 & 0 & 0 \end{pmatrix} & \begin{pmatrix} \mu & 0 & 0 \\ 0 & \lambda+2\mu & 0 \\ 0 & 0 & \mu \end{pmatrix} & \begin{pmatrix} 0 & 0 & 0 \\ 0 & 0 & \lambda \\ 0 & \mu & 0 \end{pmatrix} \\ \begin{pmatrix} 0 & 0 & \mu \\ 0 & 0 & 0 \\ \lambda & 0 & 0 \end{pmatrix} & \begin{pmatrix} 0 & 0 & 0 \\ 0 & 0 & \mu \\ 0 & \lambda & 0 \end{pmatrix} & \begin{pmatrix} \mu & 0 & 0 \\ 0 & \mu & 0 \\ 0 & 0 & \lambda+2\mu \end{pmatrix} \end{pmatrix}$$

This adaptive finite element code provides automatic grid refinement during the calculation in order to compute solutions with high accuracy. The linear algebraic systems inherent in the finite element method is solved by the conjugate gradient method [9] combined with an incomplete LU-decomposition as preconditioner. This iterative procedure is started with the solution of the previous level as an initial guess. Adaptive grid refinement and preconditioned solution on each level of refinement establishes what we call a multilevel solver.

After successful FEM–calculation, the results are transferred to AMIRA for visualization.

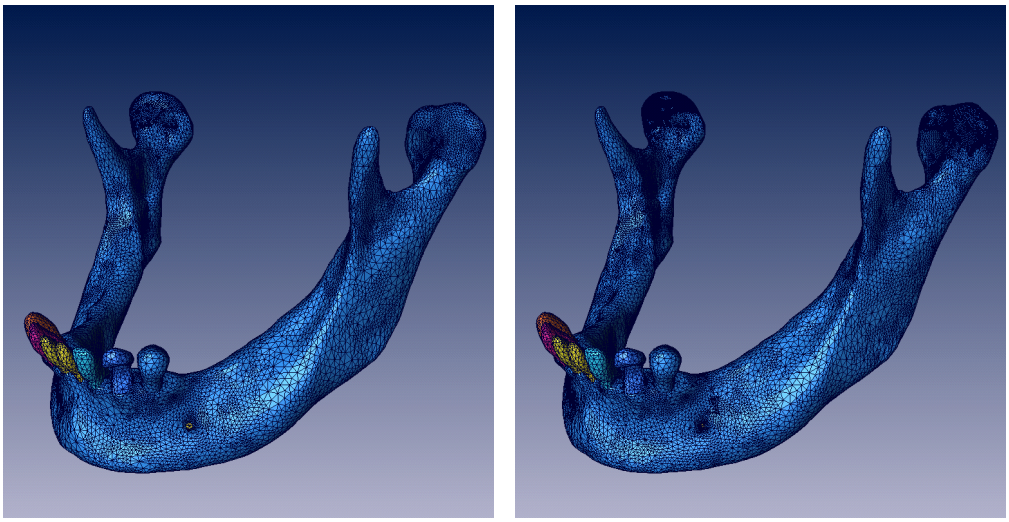

Figure 3: Initial grid (left) and adaptive mesh (right) after two steps of refinement.(TMJ capsules are not drawn.)

step	Points	x-Deformation	y-Deformation	z-Deformation
0	36802	-4.86e-5 - 2.39e-5	-6.08e-5 - 1.34e-5	-6.64e-6 - 6.43e-5
1	74696	-5.29e-5 - 2.52e-5	-6.31e-5 - 1.41e-5	-6.92e-6 - 6.73e-5
2	138890	-5.29e-5 - 2.56e-5	-6.34e-5 - 1.43e-5	-7.04e-6 - 6.77e-5
3	311206	-5.36e-5 - 2.59e-5	-6.38e-5 - 1.43e-5	-7.08e-6 - 6.82e-5
4	708879	-5.58e-5 - 2.61e-5	-6.48e-5 - 1.45e-5	-7.13e-6 - 6.93e-5

Table 1: Minima/maxima of displacement components during adaptive refinement.

To illustrate the effects of the adaptive method we present some results from our simulation using the elastic parameters as mentioned in Section 2.3. Figure 3 shows the initial grid and the grid after of two steps of adaptive refinement. At first sight this is not very impressive, because the initial grid has already quite a fine resolution. However, we easily recognize the refinement on the interface of tmj capsules and mandible due to extremely different material properties. Furthermore, a detailed analysis shows that the adaptive refinement is exactly in those regions where the accuracy of the solution is essentially improved.

step	points	σ_{vM}
0	36802	1.17e+7
1	74696	1.54e+7
2	138890	1.56e+7
3	311206	1.61e+7
4	708879	2.00e+7

Table 2: Maximum von Mises stress during adaptive refinement.

Tables 1 and 2 show the development of the minima/maxima of the displacement components and the maxima of the von Mises stress during the adaptive refinement process. The von Mises stress is defined by

$$\sigma_{vM} = \frac{1}{\sqrt{2}} \left[(\sigma_{11} - \sigma_{22})^2 + (\sigma_{22} - \sigma_{33})^2 + (\sigma_{11} - \sigma_{33})^2 + 6(\sigma_{12}^2 + \sigma_{23}^2 + \sigma_{13}^2) \right]^{1/2}$$

step	Points	x-Deformation	y-Deformation	z-Deformation
0	36802	-3.99e-4 - 3.59e-4	-1.18e-3 - 1.32e-4	-8.72e-5 - 1.17e-3
1	72719	-4.19e-4 - 3.29e-4	-1.23e-3 - 1.42e-4	-9.24e-5 - 1.23e-3
2	135052	-4.24e-4 - 3.45e-4	-1.23e-3 - 1.43e-4	-9.27e-5 - 1.24e-3
3	292090	-4.44e-4 - 3.38e-4	-1.24e-3 - 1.43e-4	-9.30e-5 - 1.24e-3
4	648464	-4.43e-4 - 3.46e-4	-1.24e-3 - 1.43e-4	-9.28e-5 - 1.24e-3

Table 3: Minima/maxima of displacement components during adaptive refinement. E=0.1 MPa in the capsules.

We can state a clear improvement of the results during the four adaptive refinement steps, but not yet convergence. In another calculation based on softer tmj capsules ($E = 0.1$ MPa), the convergence is obvious, see Tables 3 and 4.

To get the same reliability of the results when using a method only equipped with uniform refinement the amount of computational resources would be in another order of magnitude, compare our former investigations in [7].

Though in a lot of mechanical computations finite elements of higher order of convergence are preferred, we could show in our application that linear finite elements are sufficiently accurate if they are combined with adaptive grid control.

step	points	σ_{vM}
0	36802	9.19e+7
1	72719	1.49e+8
2	135052	1.50e+8
3	292090	1.50e+8
4	648464	1.50e+8

Table 4: Maximum von Mises stress during adaptive refinement. E=0.1 MPa in the TMJ capsules.

2.3 Structural mechanics simulation

The condyles are embedded into simplified temporo mandibular joint capsules where they are freely mobile. The capsules' bonding to the skull is modeled by rigid attachment.

As an example, we simulate a lateral bite on the left premolar. Our focus is the mandibular ramus. Thus we assume the "biting tooth" as nearly non deformable by muscular forces towards a very hard item to be crunched. Therefore, within this pilot study, we keep this tooth fixed.

As a first approximation, we keep the whole setting as simple as possible: we choose an isotropic material law and assume piecewise homogeneity for all involved materials. According to [7], we set as average value for the Young modulus E = 13.3 GPa for cortical, E = 1.33 GPa for spongy bone, and E = 16.0 GPa for the teeth. The Poisson ratio is assumed to be 0.224 for both constituents of bone and for the teeth. Newer biomechanical research proves that the temporomandibular joint discs are viscoelastic or even poroelastic, see for instance [21, 3]. In our macroscopic model, at least at the moment, we set aside this fine differentiation. In [21], the Young modulus of canine discs is reported as between 30.9 MPa and 15.8 MPa. In order to meet at least the order of magnitude, we choose E = 20 MPa for the temporomandibular joint capsules. The Poisson ratio is set $\nu = 0.3$.

	masseter	temporalis	pteryg.medialis	pteryg.lateralis
biting side	91	81	43	0
balancing side	60	68	29	0

Table 5: Muscular forces [N].

As reported in Section 2.1, the four respectively eight common masticatory muscles were included in the simulation. These are the musculi masseter,

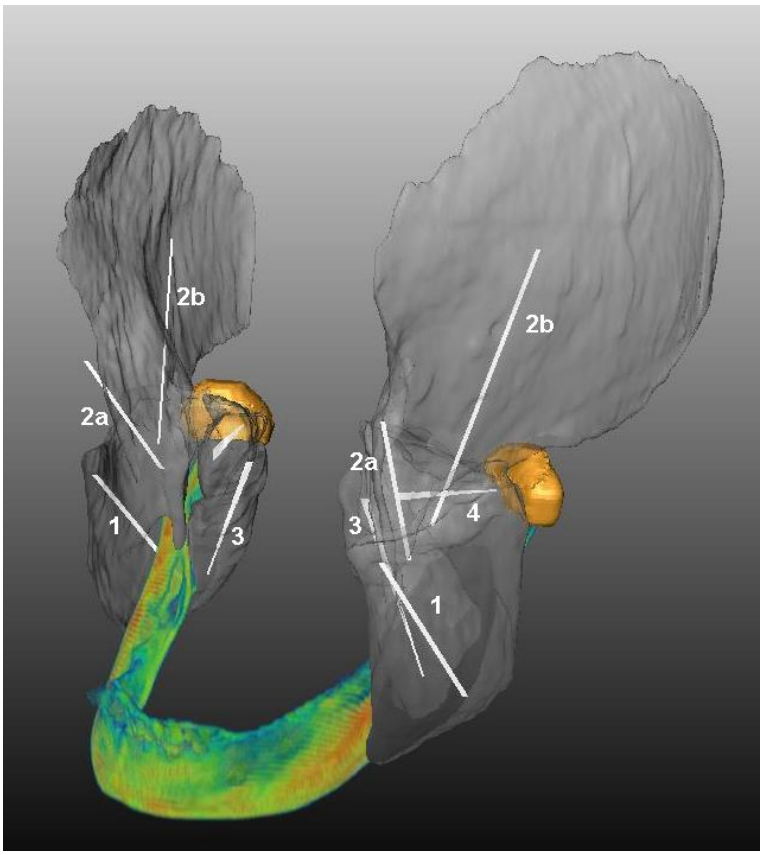

Figure 4: Surface reconstruction of the masticatory muscles and their direction vectors (1: Musc. masseter, 2: Musc. temporalis, 2a: pars anterior, 2b: pars posterior, 3: Musc. pterygoidei mediales, 4: Musc. pterygoidei laterales); mandible: visualization of the density by volume rendering.

the musculi temporales, the musculi pterygoidei mediales, and pterygoidei laterales, see Figure 1 or Figure 4. For muscular forces, we refer to the data given in [15] which base on electromyographic measurements, see Table 5. The direction vectors applied in our simulation were extracted from the surface reconstruction, see Figure 4. In this preliminary study, we confined ourselves to constant direction vectors for each muscle.

2.4 Comparison of the simulation results and the inner structure of the jaw bone

Based on Hounsfield values coming from the ct–data a three dimensional volumetric visualization of bone mineral density can be given, for details see [12].

The first step is transparent rendering of the organ under consideration without colour. Therein, regions of different density were also transparently rendered, but coloured according to their optical density. This allows to study regions of atrophied bone in their spatial context. Usually, we follow the physical colour scale which means that red stands for high density whereas dark blue indicates the lowest level. The steps are dark blue (lowest level) – light blue – green — yellow – orange – red (highest level). See Figure 6 or 7 for examples.

As a preliminary but less significant step, volume rendering using an adapted colour map can be applied, see for instance Figure 4 or 5.

The correlation of Hounsfield–values and bone mineral density is an actual topic of biomedical research, see for instance ct–osteoabsorptiometry in [14]. The appropriate visualizations are mostly two dimensional and refer to one or more cross sections of the ct–data.

Within this setting, a qualitative comparison of the density profile and the stress/strain distribution caused by selected load cases is possible. Regions of elevated stress respective strain level should be compared with regions of elevated tissue density and vice versa. Especially, correlations of weakened regions of reduced density and elevated compression (negative strain) are to be studied.

3 Results

As pointed out in the last section, we want to detect qualitative correspondences of the inner structure of the jaw to the loading situation due to the masticatory movement. This means for example that we can state higher density where the simulation indicates increased loading.

One step further, we have to face the question which one of the multitude of postprocessing variables, e.g., von Mises equivalent stress or hydrostatic pressure, is to be evaluated in order to obtain significant results. In our framework, we start with two classical ones which are volumetric strain and

von Mises equivalent stress, also with regard to our still isotropic material law.

Very generally, concerning the simulation results, we discern three regions of different stress/strain levels: the region around the teeth, the mandibular ramus, and the mandibular condyles. The region near the "biting tooth" exhibits for both postprocessing variables the highest values whereas at the condyles the lowest values occur.

3.1 Inner architecture versus volumetric strain

In contrast to von Mises equivalent stress, volumetric strain is a signed post-processing variable. By this, we can differ compression with negative sign and dilatation with positive sign.

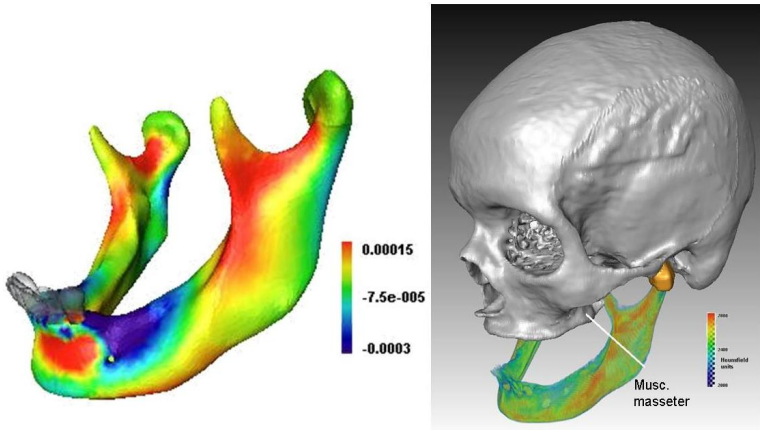

Figure 5: Volumetric strain for a lateral bite(left); skull, capsules, mandible: visualization of the density by volume rendering (right).

Figure 5 shows at the left hand side the strain profile occurring at a lateral bite according to the simulation concept described in Section 2. To the right, a visualization of the density of the mandible is given by means of volume rendering with an adapted colour scale.

The first remarkable feature is the dominant compression at the alveolar process besides the biting tooth. This corresponds to reduced density there, see Figure 5.

Next, we can state high dilatation at the mandibular notch, following the oblique line and the lower part of the coronoid process roughly correlated to elevated density in this region. At the condyles, low strain level is in

qualitative agreement with low density. The same is true for the middle part of the mandibular ramus. For the anatomical terms, see Figure 1.

3.2 Inner structure versus von Mises equivalent stress

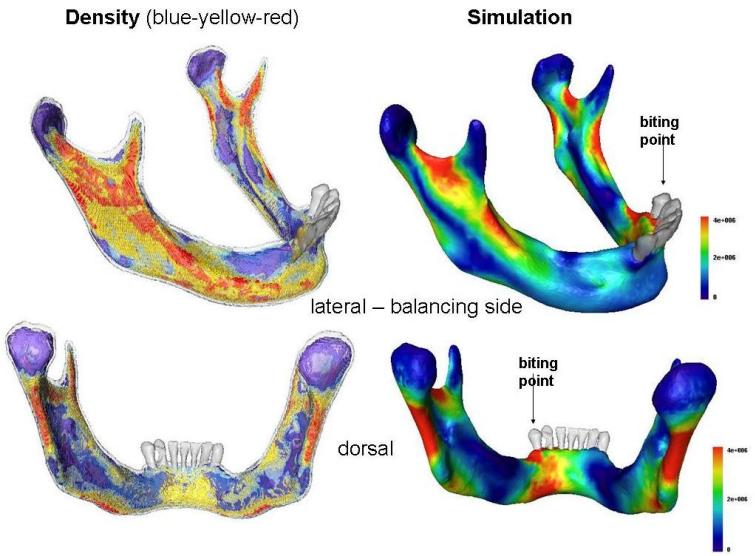

Figure 6: Von Mises equivalent stress versus inner structure, density visualization account to [12].

Von Mises equivalent stress is one of the most common and most distinguished postprocessing variables to characterize elastic material behaviour, especially if the tissue is isotropic. Because at this stage of the project we refrained from anisotropic simulation, von Mises equivalent stress should be dedicated to the comparison with the density profiles, see Figure 6.

We can state correspondences of stress to density at both rami (working and balancing side), at the condyles, and at the mandibular notch, medial and lateral. Contrary to volumetric strain, see Section 3.1, the high density at the posterior part of the ramus is in good agreement with the increased stress values. But we get disagreement at the coronoid process.

The dorsal view of the density visualization shows elevated values below the incisors indicated by yellow colour. Our simulated lateral bite caused increased stress according to the appropriate "biting tooth" deferred to the left. This shift may indicate that the person in her lifetime may have used the incisors more than the premolar where our lateral bite is situated.

A short annotation again concerning the dorsal view of the inner structure should be added. The regions with high density at the bottom side of the alveolar process may be correlated to the traction of the musculi mylohyoidei and geniohyoidei which were not included to the simulation.

3.3 The pars posterior of the musculus temporalis

According to Figure 5, the high positive strain values at the anterior part of the coronoid process correspond to elevated densitiy values there. The high strain values follow the mandibular notch up to the condyle. According to our hypothesis, we also expect high density values there. But, at the posterior part of the coronoid process, we can state a small spot of reduced density. Within our framework, this should correlate with elevated compression.

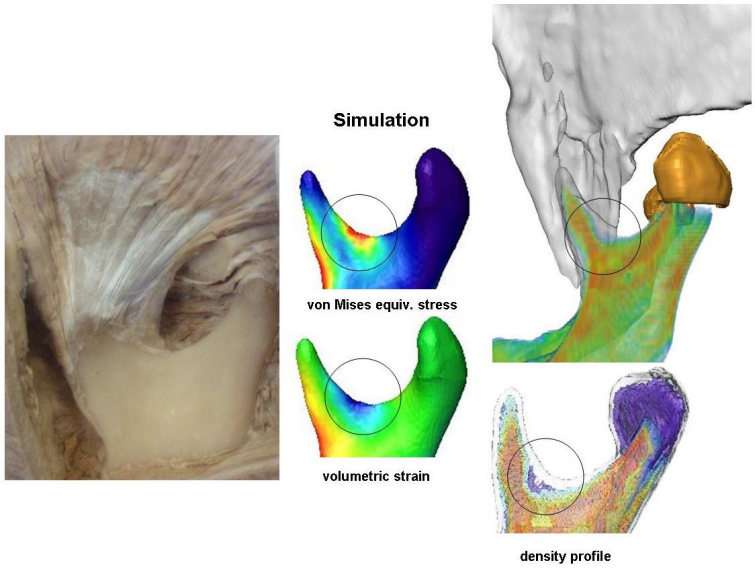

Figure 7: Correspondence of reduced density to elevated compression at the posterior part of the coronoid process. (Anatomical dissection: Anatomische Anstalt, Univ. Munich, photograph: C. Kober)

For the simulations presented in the previous sections, the direction vector of the musculus temporalis was chosen according to its anterior part. Motivated by the observations cited above, we change this direction vector to the posterior part of the musculus temporalis. Thereafter, the simulation results, the strain profile as well as the von Mises equivalent stress, show the expected qualitative agreement, see Figure 7.

4 Discussion and outlook

We detected various qualitative correspondences of the mandible's density profile to the simulated stress/strain profiles but also, in some cases, disagreement. The latter may be caused by wrong assumptions or inadmissible simplifications concerning our simulation model. A significant example has already been identified by the simulations given in the Sections 3.1 and 3.3: constant direction vectors especially for the musculus temporalis lead to incomplete results at the posterior part of the coronoid process. Further, the boundary conditions at the "biting tooth" should be taken into account. Its fixation is not realistic in the sense that very small displacements there can be measured during biting. Finally, the assumption of an isotropic material law and the homogeneity of cortical and cancellous bone should be cited as severe simplifications of the model. By these lines, the areas of further investigation are clear: a more realistic design of the direction vectors of the muscles, improved boundary conditions at the tooth, and anisotropic and fully inhomogeneous simulation. See [10] for first results.

The relevant load cases to our project are standard situations occurring often and thus influencing the inner structure of bone. It is very likely, that human individuals do not exhibit only one biting habit but a variety of those. We cannot expect to capture the whole spectrum practised by our test person considering only one biting situation. Therefore, an important part of our future work will be dedicated to additional biting scenarios as for instance teeth clenching.

Finally, there is a third point, we want to discuss in this context. Geometry reconstruction, see Section 2.1, was quite refined and adapted to the test person's individuality. But, even the material law, besides the separation of cortical and cancellous bone, does not exhibit any individual feature of the patient. Muscle directions were individually averaged over the whole muscle attachment. Muscle forces were set according to quite sophisticated electromyographic measurements [15], but nevertheless without any relation to the test person. Summing up, we compare a quite general simulation setting with the definitely individual density profile.

But in spite of these limitations, many significant qualitative correspondences of the density profile to the stress/strain profiles could be stated. This motivates the question whether there is general "jaw like" loading situation independent of individual features.

In the long run, these observations may enable the use of the simulation for diagnosis and prognosis. An important step will be the application to data

sets of real patients.

5 Acknowledgement

The first author wants to thank the "AMIRA–group" at the Zuse Institut, especially Hans–Christian Hege and Detlev Stalling, for the license of AMIRA 3.0. For his help concerning the photographs of the anatomical dissections, see Figure 7, we acknowledge Volker Kuhn, Anatomische Anstalt, University of Munich. Furthermore we want to express our sincere appreciation to Peter Deuflhard, Zuse-Institut-Berlin, and Jens Lang, Technical University Darmstadt, who provided the numerical platform for our FEM simulation and gave support by many fruitful discussions.

References

[1] `http://www.zib.de/SciSoft/kaskade`

[2] National Library of Medicine. The Visible Human Project, `http://www.nlm.nih.gov/research/visible/visible_human.html`, 1995.

[3] M. Beek, J.H. Koolstra, T.M. van Eijden: Human temporomandibular joint disc cartilage as a poroelastic material, Clin. Biomech., Bristol/Avon, 18(1), 2003, pp. 69-76.

[4] F. Bornemann, B. Erdmann, R. Kornhuber: Adaptive multilevel-methods in three space dimensions, Int. J. Num. Meth.in Eng, Vol. 36, (1993), pp. 3187-3203.

[5] P. Deuflhard, P. Leinen, H. Yserentant: Concepts of an Adaptive Hierarchical Finite Element Code. IMPACT Comp. Sci. Eng. 1 (1989), pp. 3-35.

[6] B. Erdmann, J. Lang, R. Roitzsch: KASKADE–Manual, Technical Report TR 93-05, Konrad–Zuse–Zentrum Berlin (ZIB), 1993.

[7] B. Erdmann, C. Kober, J. Lang, P. Deuflhard, H.-F. Zeilhofer, R. Sader: Efficient and Reliable Finite Element Methods for Simulation of the Human Mandible, Proceedings of 9th Workshop on The Finite Element Method in Biomedical Engineering, Biomechanics and Related Fields, CDRom, Ulm, Germany, July 2002.

[8] H. Gray: Anatomy of the Human Body, http://www.bartleby.com/107/.

[9] M.R. Hestenes, E. Stiefel: Methods of Conjugate Gradients for Solving Linear Systems, J. Res. Nat. Bur. Stand. 49 (1952), pp. 409-436.

[10] C. Kober, R. Sader, H.-F. Zeilhofer, P. Deuflhard: An Individual Anisotropic and Inhomogeneous Material Description of the Human Mandible. to appear in the Proceedings of ECMTB2002, Milano, Italy, July 2002.

[11] C. Kober, R. Sader, H.-F. Zeilhofer: Multimodal Preprocessing for Human Biting Simulation, Proceedings of 9th Workshop on The Finite Element Method in Biomedical Engineering, Biomechanics and Related Fields, CDRom, Ulm, Germany, July 2002.

[12] C. Kober, R. Sader, H.-F. Zeilhofer: Segmentation and visualization of the inner structure of craniofacial hard tissue, in Proc. Comp. Ass. Rad. Surg., London, Vol. 1256 (2003), pp. 1257-1262.

[13] J. Lang: Adaptive Multilevel Solution of Nonlinear Parabolic PDE Systems, Lecture Notes in Computational Science and Engineering, Hrsg.: M. Griebel, D.E. Keyes, R.M. Nieminen, D. Roose, T. Schlick, Springer, 2000.

[14] M. Müller–Gerbl: The subchondral bone plate, Adv. Anat. Embryol. Cell Biol.,141:III-XI (1998), pp. 1-134.

[15] Q. Rong: Finite Element Simulation of the Bone Modeling and Remodeling Process around a Dental Implant, Ph.D. Thesis, Universität Karlsruhe, June 2002.

[16] D. Stalling, M. Westerhoff, H.-C. Hege: Amira – an objectoriented system for visual data analysis. In C. Johnson, C. Hansen (Eds.), Visualization Handbook, Academic Press, to appear 2003.

[17] M. Seebaß, R. Beck, J. Gellermann, J. Nadobny, P. Wust: Electromagnetic phased arrays for regional hyperthermia – optimal frequency and antenna arrangement, Report 00-28, Konrad–Zuse–Zentrum Berlin (ZIB), 2000.

[18] D. Stalling, M. Seebass, S. Zachow: Mehrschichtige Oberflächenmodelle zur computergestützten Planung in der Chirugie, Technical Report TR 98-05, Konrad–Zuse–Zentrum Berlin (ZIB), 1998.

[19] D. Stalling, M. Zöckler, H.-C. Hege: Segmentation of 3D Medical Images with Subvoxel Accuracy, in: H.U. Lemke, K. Inamura, M.W. Vannier, A.G. Farman (eds), Proc. CAR'98 Computer Assisted Radiology and Surgery, Tokyo, 1998, pp. 137-142.

[20] D. Stalling, M. Zöckler, H.-C. Hege: AMIRA – Advanced Visualization, Data Analysis and Geometry Reconstruction. `http://amira.zib.de`.

[21] E. Tanaka, M. Tanaka, Y. Miyawaki, K. Tanne: Viscoelastic properties of canine temporomandibular joint disc in compressive load-relaxation, Arch. Oral Biol., 1999, 44(12), pp. 1021-1026.

[22] J. Wolff: Das Gesetz der Transformation der Knochen, Hirschwald Berlin, 1892.